

Radiation damping at clinical field strength: Characterization and compensation in quantitative measurements

Niklas Wallstein¹  | Roland Müller¹  | André Pampel¹  | Harald E. Möller^{1,2}  

¹Nuclear Magnetic Resonance Methods & Development Group, Max Planck Institute for Human Cognitive and Brain Sciences, Leipzig, Germany

²Faculty of Physics and Earth Sciences, Felix Bloch Institute for Solid State Physics, Leipzig University, Leipzig, Germany

Correspondence

Niklas Wallstein, Nuclear Magnetic Resonance Methods & Development Group, Max Planck Institute for Human Cognitive and Brain Sciences, Stephanstraße 1a, 04103 Leipzig, Germany.
Email: wallstein@cbs.mpg.de

Funding information

International Max Planck Research School on Neuroscience of Communication: Function, Structure, and Plasticity (IMPRS-NeuroCom)

Abstract

Purpose: In any MR experiment, the bulk magnetization acts on itself, caused by the induced current in the RF receiver circuit that generates an oscillating damping field. This effect, known as “radiation damping” (RD), is usually weak and, therefore, unconsidered in MRI, but can affect quantitative studies performed with dedicated coils that provide a high SNR. The current work examined RD in a setup for investigations of small tissue specimens including a quantitative characterization of the spin-coil system.

Theory and Methods: A custom-made Helmholtz coil (radius and spacing 16 mm) was interfaced to a transmit-receive (Tx/Rx) switch with integrated passive feedback for modulation or suppression of RD similar to preamplifier decoupling. Pulse sequences included pulse-width arrays to demonstrate the absence/ presence of RD and difference techniques employing gradient pulses or composite RF pulses to quantify RD effects during free precession and transmission, respectively. Experiments were performed at 3T in small samples of MnCl_2 solution.

Results: Significant RD effects may impact RF pulse application and evolution periods. Effective damping time constants were comparable to typical T_2^* times or echo spacings in multi-echo sequences. Measurements of the phase relation showed that deviations from the commonly assumed 90° angle between the damping field and the transverse magnetization may occur.

Conclusion: Radiation damping may affect the accuracy of quantitative MR measurements performed with dedicated RF coils. Efficient mitigation can be achieved hardware-based or by appropriate consideration in the pulse sequence.

KEYWORDS

dedicated RF coils, qMRI, radiation damping, relaxometry, spin-coil interaction

1 | INTRODUCTION

Achieving a high SNR is challenging in MR of specimens that are small compared to the sensitive volume of standard receiver coils.^{1,2} In such cases, dedicated coils with an increased “filling factor” η and quality factor Q are often employed. However, this may concomitantly result in relevant radiation damping (RD)^{3–12} caused by inductive coupling of the bulk magnetization and the coil, that is, the processing magnetization interacts with itself mediated by the detection circuit. According to Lenz’s law, the induced current generates an oscillating damping field that rotates the magnetization without altering its length. A well-known RD effect is an increased linewidth of strong signals (e.g., solvent peaks) in high-resolution NMR.^{11,13,14} Despite a common assumption, RD is not unique to high magnetic fields,⁹ but has been observed in NMR at lower fields^{3–5} and occasionally MRI at clinical field strength.^{15,16}

Previous works have described RD in various experiments,^{12,16–24} including relaxation and magnetization-transfer (MT) measurements, perfusion MRI, spectroscopy, and more. Of note, RD is not only present during free precession (with or without signal detection), but also during RF transmission.^{7,25} Here, RD is more difficult to characterize and may interfere with the desired magnetization trajectory during the pulse, thereby altering the effective flip angle θ_{eff} . Damping during transmission is more prominent for long, low-power pulses with durations τ_p of several milliseconds.

Various techniques have been proposed for mitigating, suppressing or even utilizing²⁶ RD, including a reduced sample region contributing to the signal,²¹ small flip-angle pulse trains to counterbalance RD,²⁷ coils with switchable Q ,²⁸ or active electronic feedback.²⁹ Most methods rely on gradient pulses to minimize coherent transverse magnetization.^{16,20,30–32} If this is not applicable (e.g., during RF pulses), alternative solutions are required.^{7,25} Approaches to obtain RD-insensitive RF pulses were based on theoretical considerations,³³ composite pulses and gradient optimization,⁷ or optimal-control theory.³⁴

Currently, little is known how RD might confound the accuracy of quantitative MRI, which is increasingly used to study tissue microstructure or composition (e.g., myelin or iron content).³⁵ As more prominent perturbations result with high η and Q , unconsidered damping-related bias may be of particular concern when scanning small specimens with bespoke RF coils. This is a typical approach for correlating results from MRI and other modalities.^{36,37} For example, investigations in fixed marmoset brain yielded cortical T_1 values ranging from 371 ms at the gray-white matter boundary to 359 ms in the stria of Gennari, corresponding to a variation of only 3.2%.³⁷ This underscores the degree of precision required to identify the

gross signature of cortical layers using relaxation measurements. Small effect sizes are also characteristic of other MRI experiments, for example, arterial spin labeling¹⁶ or MT^{22,37} and relaxation anisotropy measurements in white matter,^{38,39} indicating that their performance may be impacted by RD. Damping effects were also observed in reference measurements of T_1 of blood with a standard transmit-receive (Tx/Rx) head coil.⁴⁰ The focus of the current work was, therefore, on a comprehensive characterization of RD in simple phantoms employing a setup for small samples on a clinical scanner. The degree of damping was externally adjusted through a hardware modification. Finally, RD was independently quantified for free precession and transmission.

2 | THEORY

To account for RD, the evolution of the magnetization is described by augmenting the Bloch equations by: an additional back-action field \mathbf{B}_{RD} .⁵ Its amplitude is proportional to the (complex) transverse magnetization $M_+ = M_x + iM_y$:

$$\mathbf{B}_{\text{RD}} = i \frac{\zeta}{\gamma} e^{-i\psi} M_+ \quad (1)$$

where γ is the gyromagnetic ratio. ζ is the damping rate, which depends on the characteristics of the RF circuit:

$$\zeta = \frac{\mu_0 \gamma |\omega_0| \eta L}{2|Z(\omega_0)|} \quad (2)$$

with

$$|Z(\omega_0)| = \frac{\omega_{\text{LC}} L}{Q} \sqrt{1 + 4\Delta_{\text{LC}}^2} \quad (3)$$

$$\Delta_{\text{LC}} = Q \frac{\omega_0^2 - \omega_{\text{LC}}^2}{\omega_0 \omega_{\text{LC}}} \quad (4)$$

and

$$\psi = \arctan \Delta_{\text{LC}} \quad (5)$$

where μ_0 is the vacuum permeability, L the coil’s inductivity, ω_0 the Larmor frequency, and ω_{LC} the circuit’s resonance frequency. The RD field lags behind the transverse magnetization by an angle $\pi/2 - \psi$, that is, both are in quadrature for a perfectly tuned coil with $\Omega \equiv \omega_0 - \omega_{\text{LC}} = 0$. The (complex) nutation frequency $\omega_{\text{RD}} = -\gamma \mathbf{B}_{\text{RD}}$ has, therefore, components

$$\omega_{\text{RD},x} = -\gamma B_{\text{RD},x} = -\zeta (M_x \sin \psi - M_y \cos \psi) \quad (6a)$$

$$\omega_{\text{RD},y} = -\gamma B_{\text{RD},y} = -\zeta (M_x \cos \psi + M_y \sin \psi) \quad (6b)$$

This notation is slightly different from recent work^{10,12} but follows Vlassenbroek et al.^{6,14} With $\omega_1 = -\gamma \mathbf{B}_1$, the

combined spin-coil system is, hence, described by the Bloch-Maxwell equations in the rotating frame as:

$$\frac{dM_x}{dt} = -\Omega M_y + \omega_{1y} M_z + \omega_{RD,y} M_z - \frac{M_x}{T_2} \quad (7a)$$

$$\frac{dM_y}{dt} = \Omega M_x - \omega_{1x} M_z - \omega_{RD,x} M_z - \frac{M_y}{T_2} \quad (7b)$$

$$\frac{dM_z}{dt} = -\omega_{1y} M_x + \omega_{1x} M_y - \omega_{RD,y} M_x + \omega_{RD,x} M_y - \frac{M_z - M_0}{T_1} \quad (7c)$$

Often, an effective damping time constant τ_{RD} is used as an indicator of the RD strength. It is related to ζ by:

$$\tau_{RD} = \frac{1}{\zeta M_0 \cos \psi} \quad (8)$$

To account for static field inhomogeneities, T_2 is commonly replaced by T_2^* .¹³ However, this simplification may not capture transient RD effects,^{9,41} and an approach based on isochromats may be preferable in some cases.^{6,9,14,41}

3 | METHODS

All experiments were performed at 3 T on a MAGNETOM Skyra^{fit} (Siemens Healthineers, Erlangen, Germany) operated under the software baseline *syngo* MR VE11E. Various tailored pulse sequences were developed to ensure sufficient experimental flexibility.⁴² They provide a variety of RF pulse types for preparation, excitation and refocusing, whereby every pulse may be spatially selective or non-selective. Different preparation schemes (excitation, saturation, inversion) are supported followed by an adjustable relaxation period including variable crusher gradients. Selectable readout types included a simple FID, a spin-echo train, or multiple-echo (ME) gradient-recalled echoes (GRES).

Two spherical phantoms were used for the measurements with inner diameters of 19 and 24 mm. They were filled with aqueous $MnCl_2$ solution from the same batch. The concentration (0.135 mM) was adjusted to produce a T_1 of approximately 770 ms at room temperature.⁴³

3.1 | Helmholtz coil

A linear Tx/Rx Helmholtz coil was used in all experiments (Figure 1A).⁴⁴ It was optimized for small ex-vivo specimens to obtain a high SNR and B_1 homogeneity and short RF pulse durations ($\approx 20 \mu s$ for $\theta=90^\circ$). Most

mechanical parts were designed with CAD software and 3D-printed (Objet Eden260VS; Stratasys, Eden Prairie, MN, USA) using Objet MED610 Biocompatible Clear material (Stratasys). The final coil consisted of two loops of 2 mm diameter silver-plated copper wire connected in series. Radius and spacing of the loops were 16 mm. Bench-top measurements yielded $Q \approx 470$ of the empty coil.

For initial tests, the loaded coil was connected to a standard Tx/Rx switch via a 50Ω coaxial cable of random length. Initial experiments indicated characteristic RD effects with potential impact on the precision of quantitative experiments. They included an echo-like signal build-up after flip angles $>90^\circ$ (Figure S1) and flip-angle dependent line broadening, which was not improved by shimming. Hardware-based methods to minimize RD, such as a small η , active electronic feedback or detuning, were discarded due to reduced SNR or high circuit complexity. Alternatively, the very low input impedance of GaAs field-effect transistor (FET)-based preamplifiers at optimal noise matching was utilized in a new Tx/Rx switch (Figures 1B and S2).⁴⁵ The basic idea for this switch was modified by (i) adding an actively biased PIN-diode switch and (ii) supplementing the LC transformer for impedance reduction in the Tx branch by a resistive voltage divider. Instead of a trimmer, fixed-value capacitors were employed to match the loaded coil to 50Ω . The GaAs-based preamplifier and the voltage divider (resistors $R_1 = 2 \Omega$ and $R_2 = 1 \Omega$) yielded a strong impedance mismatch ensuring that most of the induced signals in the coil were reflected back. An alternative setup was also realized with $R_1 = 49 \Omega$ and $R_2 = 1 \Omega$. Here, the LC transformer was not necessary; therefore, C_{s1} , C_{s2} , and L_p were omitted. This resulted in a higher voltage needed for a 180° rectangular 1 ms pulse (referred to as “reference voltage” in the following), which was undesirable for many intended applications but useful for demonstrations.

The adapted Tx/Rx switch, a suitable cable length and the impedance mismatch guaranteed that the induced current in the coil, i_{in} , and the current due to reflected power, i_{re} , were almost perfectly out of phase, leading to destructive interference. Therefore, the loop currents cancel out, and RD is minimized without SNR degradation. The required phase shift is easily adjusted by the cable length. Note that the same principle is employed for preamplifier decoupling.⁴⁶ If the cable length is extended by a quarter of the wavelength ($\lambda/4$), the loop currents reach a maximum (in-phase interference of i_{in} and i_{re}).⁴⁷ Thus, a coaxial cable of appropriate length between the coil and the Tx/Rx switch achieves changing from minimum to maximum RD with nearly identical coil characteristics. This permits convenient checks if pulse sequences are

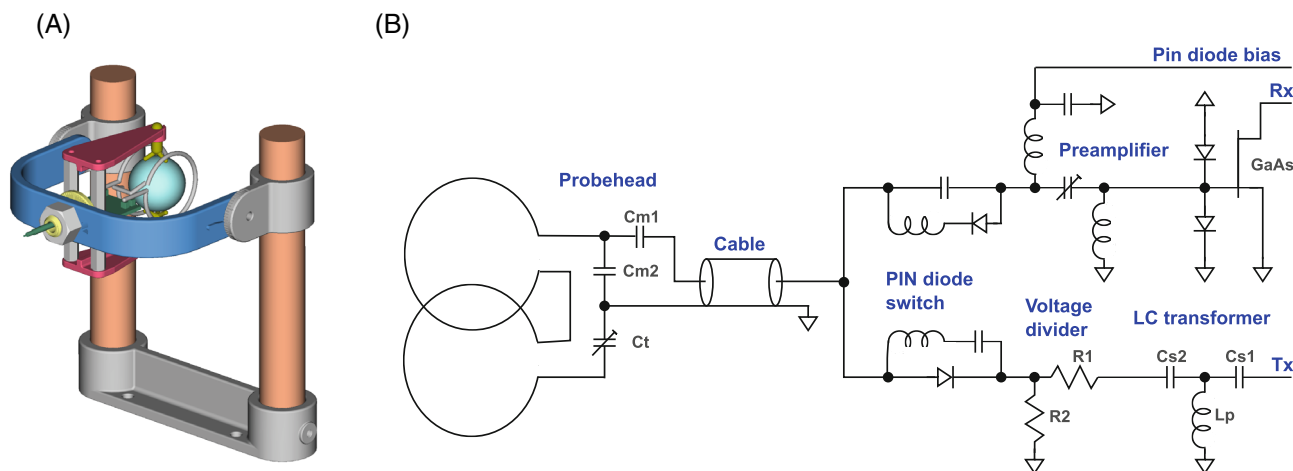


FIGURE 1 (A) Custom-built linear Helmholtz coil with a spherical water phantom. The sample holder is designed for either standard 5 mm NMR tubes or 3D-printed spherical containers up to 25 mm diameter (as shown here). For studies of orientation dependence of MR parameters (not used in the current study), it can be tilted about the x -axis and z -axes of the magnet, together with the self-supporting coil elements. Angle indications support the adjustment of a desired tilt angle. The center of the sample and the coil always remain in the magnet's isocenter upon tilting. (B) Simplified schematic of the Helmholtz coil and the Tx/Rx switch. The trimmer capacitor C_t is integrated for tuning. The required cable length for maximum radiation damping (RD) reduction depends on the choice of the (fixed) matching capacitors C_{m1} and C_{m2} . The LC transformer (C_{s1} , C_{s2} , L_p) matches the transmitter output ($50\ \Omega$) to the input impedance of the voltage divider (approximately $R_1 + R_2$). Further details are presented in Figure S1.

affected by RD or if RD suppression works. The following cables were utilized:

- 1 Optimized length for minimal RD (“*setup 1*”).
- 2 Extended length by $\lambda/6$ for moderate RD (phase-shifted interference of i_{in} and i_{re} ; “*setup 2*”).
- 3 Extended length by $\lambda/4$ for maximal RD (“*setup 3*”).

Coil tuning and matching were performed in Tx mode, using a vector network analyzer (ZVT 8; Rohde & Schwartz, München, Germany). Presumably, the Rx mode was not perfectly tuned, due to the two distinct electronic branches (Figure 1B).^{48,49} The RD-modifying cables were attached inside the scanner without retuning.

All samples were shimmed using the scanner's manual adjustment, which proved challenging due to the simultaneous presence of RD and field inhomogeneities. Therefore, shimming was performed once for *setup 1* and not readjusted after changing the cables to *setups 2* and *3*. An FWHM of 9.5 and 11 Hz was achieved for the 19 and 24 mm sample, respectively.

3.2 | Characterization of RD

Previous studies highlighted specific RD characteristics during free precession and transmission,^{10,48} suggesting a need for different experimental strategies for both coil operating modes. Therefore, individual parameters

$\tau_{RD,Rx}$, $\tau_{RD,Tx}$ as well as ζ_{Rx} , ψ_{Rx} and ζ_{Tx} , ψ_{Tx} are employed for the Rx and Tx mode, respectively.

3.2.1 | Pulse calibration and pulse sequences

According to Keifer,⁵⁰ an array of spectra acquired with an increasing pulse duration from scan to scan offers detailed characterization of the MR system, including off-resonance effects, insufficient relaxation delays, probe arcing, and so forth. Besides accurate 90° -pulse calibration, RD effects can also be visualized. In the current work, it was used to evaluate the circuit's stability and Tx-field homogeneity. Data were collected following non-selective excitation with a rectangular pulse ($\tau_p = 0.02$ – 4.42 ms). The total array consisted of 111 measurements (TR = 4.5 s). The spectra were phase-corrected, and a region of ± 1.5 ppm around the resonance position was extracted and concatenated. The array was normalized by setting the amplitude of the highest positive peak to 1.

Damping effects in T_2 measurements were investigated with non-localized Carr-Purcell-Meiboom-Gill (CPMG) sequences (adiabatic half-passage 90° and rectangular 180° pulses, $\tau_p = 1.5$ and 3 ms, respectively; 64 echoes; echo spacings $\Delta TE = 9, 11, 14, 17,$ and 20 ms; TR = 6 s). Contributions from stimulated echoes were suppressed by crusher gradients (2.5 ms; alternating sign and direction and decreasing amplitude) around each refocusing pulse.⁵¹

3.2.2 | RD during free precession

RAddition Damping Difference Spectroscopy (RADDSY) compares relaxation after a short (0.4 ms) rectangular 90° pulse in the absence and presence of RD followed by another 90° readout pulse.^{32,52} A shift of a trapezoidal crusher gradient (amplitude $G = 14$ mT/m; duration 3 ms) yields two sequence variants: (i) 90° - G - τ - 90° -ADC (undamped reference) and (ii) 90° - τ - G - 90° -ADC (damped case). The ADC (analog-to-digital converter) period indicates the time of signal detection; τ is an evolution time (between 5 and 6000 ms). If the crusher is applied immediately after the first 90° pulse, no coherent transverse magnetization is present during the evolution period, and RD is suppressed. In contrast, damping is maximal in the second sequence version, and magnetization is returned faster to the z -axis during the time τ to be detected following the second 90° pulse. In additional experiments, a 1D GRE train (48 echoes; $\Delta TE = 6$ ms, $TR = 7$ s) was utilized to measure T_2^* . The readout gradient was applied along the x -, y -, and z -axes in consecutive experiments, and the data from the three acquisitions was averaged for further analysis.

RADDSY only achieves quantitation of RD in terms of $\tau_{RD,Rx}$ without yielding information about ζ_{Rx} and ψ_{Rx} (Eq. 8). Experiments that are sensitive to ψ_{Rx} exploit the resonance shift caused by RD, that is, the imperfect quadrature alignment of the transverse magnetization and the damping field ($\psi_{Rx} \neq 0$) if the coil is not perfectly tuned.^{11,53,54} Two approaches were implemented: (i) A flip-angle array to examine the dependence of the proton frequency on θ (variation between 0° and 360° in increments of 10° ; adiabatic 5 ms BIR4-pulse⁵⁵).⁵⁴ (ii) Saturation-recovery experiments (train of six 90° pulses and crusher gradients with alternating direction, x, y, z, x, y, z , and decreasing amplitude) with different saturation levels, assuming that a weaker initial magnetization induces less RD.¹⁹ This leads to a corresponding line broadening depending on M_z accompanied by a frequency shift. Because of the long scan time (>10 min), B_0 drifts might be misinterpreted as coil detuning. Therefore, every second acquisition was replaced by a reference scan to correct for frequency shifts unrelated to RD.

3.2.3 | RD during transmission

A comprehensive characterization of RD during transmission was performed with four distinct preparation schemes consisting of two types of composite pulses. One type was designed to compensate only for inhomogeneity of the transmit field amplitude B_1^+ and off-resonance effects.⁵⁶

The other type,⁷ not only accounts for these imperfections but also compensates for RD effects. After preparation, a crusher gradient was applied, and the magnetization was read out by a $200 \mu s$ 90° pulse. We assume that differences observed with RD-compensated and uncompensated preparations primarily reflect magnitude and phase variations of the damping field during transmission and refer to this approach as RAdiation Damping Difference EXcitation (RADDEX). The following composite pulses were used in successive experiments: (i) $90_x^\circ - 315_y^\circ$ (undamped 90° rotation), (ii) $90_x^\circ - 90_y^\circ$ (damped 90° rotation), (iii) $90_x^\circ - 270_y^\circ - 90_x^\circ$ (undamped 180° rotation), and (iv) $90_x^\circ - 180_y^\circ - 90_x^\circ$ (damped 180° rotation). For each scheme, 36 measurements ($TR = 5$ s) were performed with increasing τ_p . The duration for a (rectangular) 90° subpulse in the inversion composite pulse was varied between 0.2 and 5.0 ms yielding total durations of 0.9–19.3 ms, 1.8–38.6 ms, 1.0–25.0 ms, and 0.8–20.0 ms for schemes (i), (ii), (iii), and (iv), respectively. For the 90° -excitation experiment, the maximum duration of the 315° subpulse was 15 ms (maximum duration of 4.3 ms for the 90° subpulse) in scheme (i).

To render RF pulses immune to RD, we adapted a method to modify the complex RF field describing the pulse shape in order to counterbalance the induced damping field.²⁵ This involves an iterative procedure in which the Bloch equations are initially solved to obtain $M_+(t)$ without relaxation under the assumption of an undamped RF pulse. With this result, the complex reaction field is computed with Eqs. (1), (6a), (6b) and can be canceled out by changing the nutation frequency of the amplitude and phase-modulated pulse. This procedure requires the knowledge of the RD characteristics of the investigated system. To support online application on the scanner, an interface was created on the user interface's "special card" to allow input of pre-determined RD parameters. During runtime, the Bloch-Maxwell equations were solved numerically without restriction to a perfectly tuned coil, and the rectangular pulse shape was adapted to compensate for RD. ζ_{Tx} and ψ_{Rx} were provided via the user interface, and the nutation frequencies were corrected accordingly. The RD parameters were not iteratively optimized as suggested previously²⁵ but determined by RADDEX. Instead of "pulse-width arrays," "pulse-amplitude arrays" were employed for the investigation of RD-related distortions of θ . Hence, FIDs were recorded following a 7.5 ms pulse, whose amplitude was incremented to achieve nominal flip angles varying from 0° to 360° in steps of 5° . The online compensation method improved pulse performance, which is relevant for long, low-amplitude RF pulses, and served as an indicator of the reliability of RD quantification.

3.3 | Simulations and parameter fitting

Simulations and non-linear least squares (NLLS) fitting were based on calculations of the evolution of the magnetization during the entire pulse sequence using numerical solutions of Eqs. (7a)–(7c) implemented in Matlab (R2020b; MathWorks, Natick, MA, USA). The algorithm included an ordinary differential equation solver (ode45) based on explicit Runge–Kutta formulas of orders 4 and 5. The (digitized) RF pulse shapes were directly obtained as played out during runtime from the scanner's sequence programming software (IDEA; Siemens Healthineers).^{38,57,58} The NLLS fitting used the function `nlinfit` (or also `lsqnonlin`). Confidence intervals were calculated using the `nlparci` algorithms of Matlab's Statistics and Machine Learning Toolbox (R2020). Errors are given as the 95% confidence intervals for the parameter estimates (approximately two SDs for each parameter as obtained from the covariance matrix).

A frequently used T_1 measurement is the variable flip angle (VFA) method.^{59,60} Due to RF-pulse application for each k-space line, it may be influenced by RD during transmission. Simulations were performed assuming typical relaxation times of brain tissue at 3T and body temperature (gray matter: $T_1 = 1500$ ms, $T_2 = 100$ ms; white matter: $T_1 = 900$ ms, $T_2 = 70$ ms).^{61–63} The longitudinal magnetization in a 3D spoiled GRE acquisition was calculated by solving Eqs. (7a)–(7c) for a series of 256 repetitions (TR = 30 ms) with a rectangular RF pulse.

These simulations were performed for 11 different excitation angles (between 4° and 60°) for the damped ($\tau_{RD,TX} = 17$ ms) and undamped case ($\tau_{RD,TX} \rightarrow \infty$) considering two values of τ_p (0.5 and 5 ms). Otherwise ideal conditions (ideal pulse shapes, perfect B_0 and B_1^+ homogeneity, perfect spoiling, no noise) were assumed to simplify the identification of RD effects. A typical assumption in VFA T_1 measurements is the establishment of a (periodic) steady state after a sufficiently large number of pulses (here, $N = 256$) according to the Ernst equation:⁶⁴

$$S = S_0 \frac{1 - \exp(-TR/T_1)}{1 - \exp(-TR/T_1) \cos \theta} \sin \theta \quad (9)$$

S_0 is the signal intensity obtained with $TR \gg T_1$ and $\theta = 90^\circ$. Consistently, estimates of T_1 and deviation from ground-truth input values were obtained from NNLS fits of the simulated signal intensity after the final RF pulse to Eq. (9).

4 | RESULTS

4.1 | Pulse-width arrays

Pulse-width arrays acquired with all coil setups and two spherical samples are shown in Figure 2. The results obtained with *setup 1* (Figure 2A,D) showed undistorted sinusoidal amplitude oscillations as a function of τ_p ,

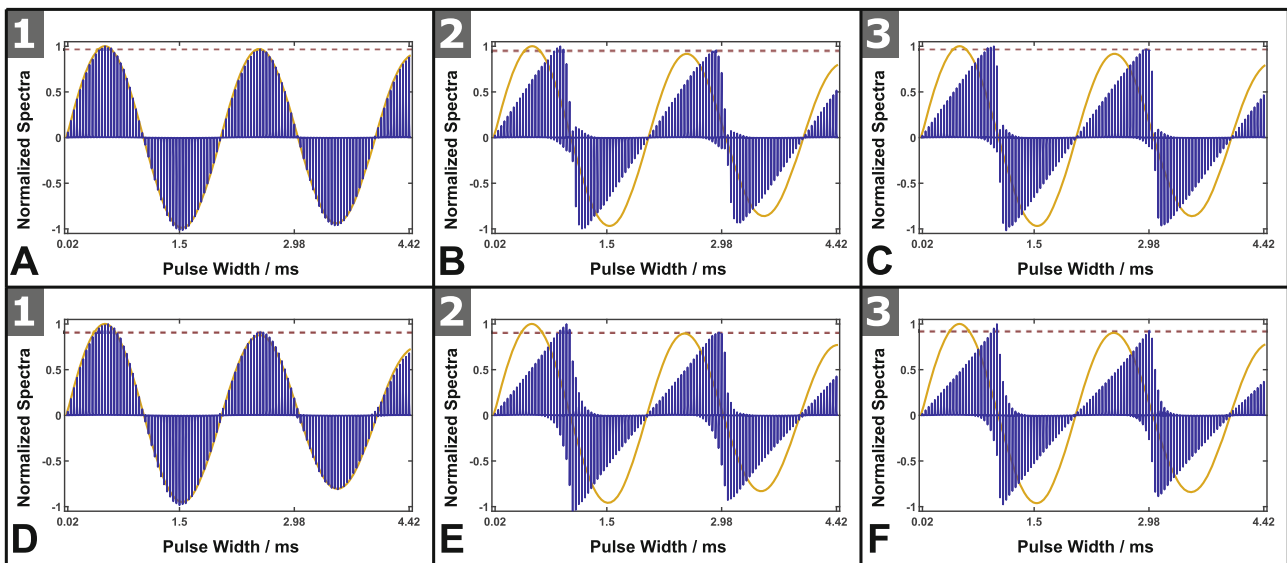


FIGURE 2 Pulse-width arrays measured with *coil setup 1* (undamped; A, D), 2 (moderately damped; B, E), and 3 (maximally damped; C, F). With all setups, the width of a rectangular pulse was stepwise increased from 0.02 to 4.42 ms at constant amplitude. (A–F) Results obtained with the spherical 19 mm sample and the 24 mm sample, respectively. Broken lines indicate the ratio of the second-highest and highest (positive) peak amplitude. Expected damped sine oscillations of the peak amplitudes for an ideal configuration are indicated by solid yellow lines. Significant deviations due to radiation damping (RD) are evident for *coil setup 2* and 3. The amplitude was adjusted to obtain a pulse length of 1 ms for a 180° pulse under ideal conditions.

TABLE 1 Summary of the reference voltages obtained by adjusting a 360° pulse with a pulse-width array for all coil setups and samples.

		Coil setup 1	Coil setup 2	Coil setup 3
Inserted cable		-	$\lambda/6$	$\lambda/4$
Damping effect		Minimal	Moderate	Maximal
19 mm sample	U_{ref}/V	17.28	16.02	16.81
	T_1/ms	770.3 ± 2.1	768.5 ± 2.0	765.7 ± 2.3
	T_2^*/ms	37.6 ± 0.2	37.5 ± 0.2	37.4 ± 0.2
	$\tau_{\text{RD,Rx}}/\text{ms}$	998 ± 60	26.5 ± 0.2	23.8 ± 0.2
	$T_2^*/\tau_{\text{RD,Rx}}$	<0.04	≈ 1.42	≈ 1.57
24 mm sample	U_{ref}/V	17.20	16.43	17.33
	T_1/ms	739.5 ± 2.6	741.2 ± 2.3	741.8 ± 2.5
	T_2^*/ms	32.7 ± 0.2	32.4 ± 0.2	32.3 ± 0.2
	$\tau_{\text{RD,Rx}}/\text{ms}$	447 ± 21	13.3 ± 0.2	12.0 ± 0.2
	$T_2^*/\tau_{\text{RD,Rx}}$	<0.08	≈ 2.44	≈ 2.69

verifying the absence of relevant RD for optimized power mismatch. These oscillations were slightly damped due to B_1^+ inhomogeneity, as evident from the amplitudes obtained with the 450° (i.e., 360° + 90°) and 90° pulse. Corresponding ratios >0.96 for the 19 mm and >0.9 for the 24 mm sample indicate excellent homogeneity.⁵⁰

In contrast to *setup 1*, substantial RD is evident for *setup 2* (Figure 2B,E) and *setup 3* (Figure 2C,F) with extended cable lengths. The oscillations are skewed, shifting the maximum positive and negative signals to flip angles >90° and <270°, respectively. These sawtooth-like profiles result from line broadening for $\theta < 90^\circ$ and distorted line-shapes between 90° and 270°.⁵⁰ The distortions are more pronounced with the 24 mm sample with increased η and magnetic moment. The 360° pulse is largely unaffected by RD⁷ and, therefore, provides a robust means to adjust the reference voltage. Corresponding results are summarized in Table 1.

4.2 | RD during free precession

Results from RADD SY experiments are shown in Figure 3. Damping effects are easily identified as deviations from an exponential recovery (blue triangles) and, correspondingly, as a difference between the damped and undamped sequence versions (black circles). Subtle RD effects are even evident in the data obtained with *setup 1*.

For quantitative analysis, magnitudes of the numerically integrated spectra were rescaled to account for small deviations from a 90° flip angle caused by relaxation or RD and residual B_1^+ inhomogeneities. This scaling factor

was determined by extrapolating the undamped recovery curve to $t = 0$. This approach reflects the z-magnetization amplitude during free evolution, whose time course was fitted to Eqs. (7a)–(7c) to estimate T_1 , T_2^* , and $\tau_{\text{RD,Rx}}$. Further important is the interplay between RD and transverse relaxation because fast dephasing may prevent an efficient rotation of the magnetization by the damping field. This is reflected in large off-diagonal elements in the covariance matrix and limits estimations of T_2^* and $\tau_{\text{RD,Rx}}$ (Pearson correlation coefficient $r > 0.96$). Therefore, additional ME-GRE acquisitions, which are sensitive to T_2^* but not to RD (due to the gradient pulses), were simultaneously fitted (combined analysis). Figure 3 demonstrates a remarkable agreement of the fits (solid lines) and experimental data, which also benefited from the high SNR.

Fitted parameters and $T_2^*/\tau_{\text{RD,Rx}}$ ratios are included in Table 1. A comparison of the samples shows that the $\tau_{\text{RD,Rx}}$ -values scale with the magnetic moments (i.e., their ratio corresponds to that of the sample volumes, 243/193 ≈ 2.02). This is expected if the increased η obtained with the larger sphere is approximately compensated by a lower Q (Eq. 8). The small T_1 difference for both samples (3%–4%) is probably due to temperature differences as the measurements were performed on different days. To avoid ambiguity, further analysis is restricted to the 19 mm sample.

To go beyond the assumption of a perfectly tuned coil, flip-angle arrays were employed to analyze the phase relation (i.e., ψ_{Rx}) between the damping field and the transverse magnetization (Figure 4), combined with ME-GRE data for estimating T_2^* . Characteristic features of the degree

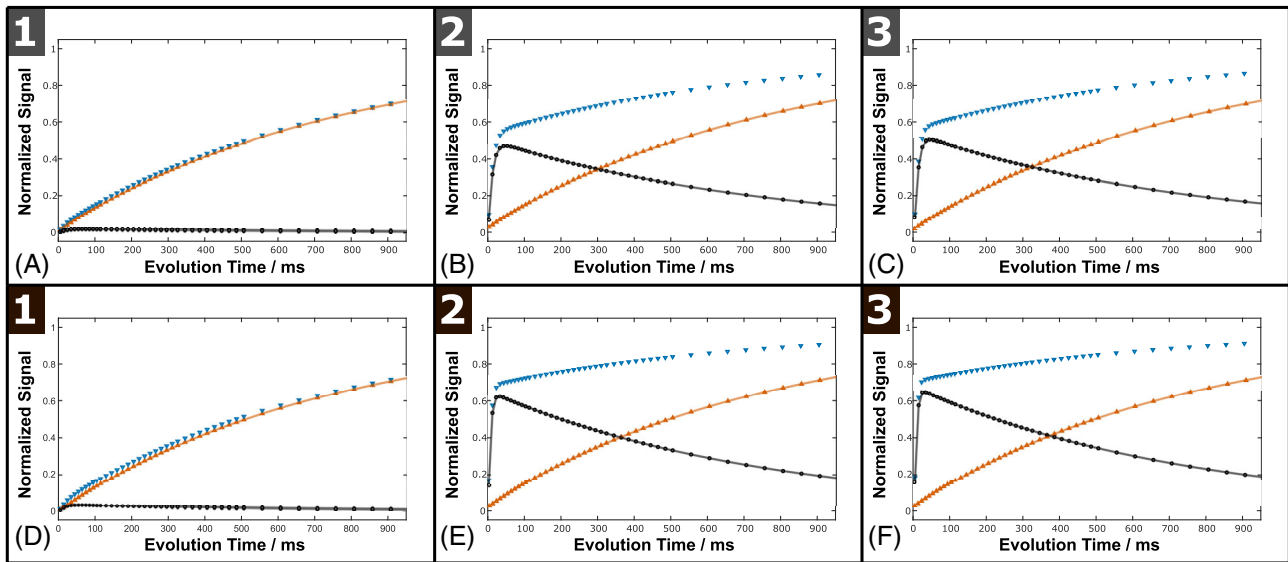


FIGURE 3 Radiation damping difference spectroscopy (RADDSY) experiments with *coil setup 1* (undamped; A, D), *2* (moderately damped; B, E), and *3* (maximally damped; C, F). (A–F) Results obtained with the spherical 19 mm sample and the 24 mm sample, respectively. The peak amplitude after full recovery (evolution time of 6 s) was set to 1 for normalization of the signals. Note that only results for evolution times below 950 ms are shown for better visualization of the effects. Blue and orange triangles show data for the two sequence variants corresponding to the damped case and undamped reference, respectively. Black circles show the difference of the two measurements. An accelerated recovery of longitudinal magnetization due to radiation damping (RD) is clearly evident for *coil setup 2* and *3*, whereas the good agreement between both sequence versions obtained with *coil setup 1* verifies conditions that are mostly free from RD (consistent with the pulse-width array results in Figure 2A,D).

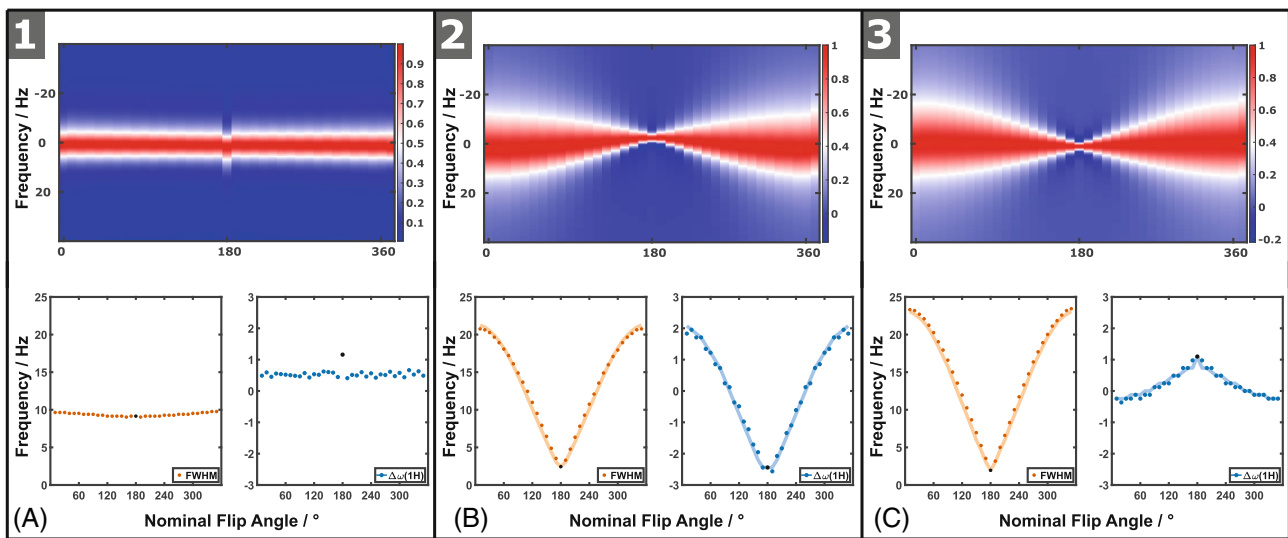


FIGURE 4 Overview of the results obtained with flip-angle arrays and the 19 mm sample with *coil setup 1* (undamped; A), *2* (moderately damped; B), and *3* (maximally damped; C). The top row shows color-coded contour plots of stacked spectra (phase-corrected real part, individually normalized to an amplitude of 1) as a function of the flip angle illustrating the changes in the peak with and position due to radiation damping (RD). The bottom row shows experimental data (colored circles) and corresponding fits (solid lines) of the FWHM (orange) and the peak position (blue).

of RD and detuning (i.e., $\omega_0 \neq \omega_{LC}$) were a dependence of the linewidth and peak position on θ . For the undamped *setup 1*, an invariant FWHM and insignificant frequency shifts verify negligible RD, consistent with the above

results. By contrast, prominent RD for *setups 2* and *3* produce distinct FWHM variations and frequency shifts, the latter being more pronounced for the maximally damped *setup 3*.

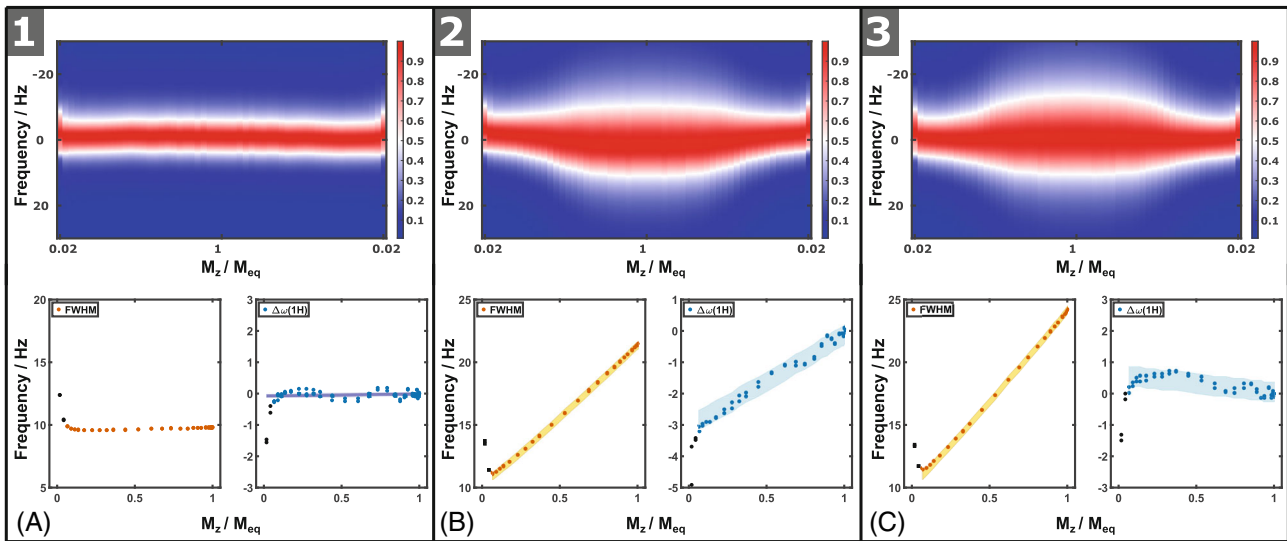


FIGURE 5 Overview of the results obtained with saturation recovery (evolution times $10 \text{ ms} \leq \tau \leq 6 \text{ ms}$) and the 19 mm sample with *coil setup 1* (undamped; A), 2 (moderately damped; B), and 3 (maximally damped; C). The results are plotted in dependence of $M_z(\tau)/M_0$ instead of τ . The top row shows color-coded contour plots of stacked spectra (phase-corrected real part, individually normalized to an amplitude of 1) as a function of the flip angle illustrating the changes in the peak with and position due to radiation damping (RD). Note that the evolution time was first increased from 10 ms to 6 s in sequential measurements and then decreased from 6 s to 10 ms. Thus, the entire series appears twice, with M_z/M_0 (on the abscissa) first increasing from 0.02 to 1 and then decreasing back to 0.02. This presentation allows a better assessment of the reproducibility of the results. The bottom row shows experimental data (colored circles) and corresponding fits of the FWHM (orange) and the peak position (blue). Shaded areas illustrate 95% confidence intervals of the fits.

For quantification, FIDs were simulated, and the FWHM and peak position were fitted considering four adjustable parameters: ζ_{RX} , ψ_{RX} , T_2^* and a frequency term δf accounting for B_0 drift. $T_1 = 770$ was a fixed parameter because it varied by $\leq 0.6\%$ in different measurements (Table 1). The results suggest that the phase term may be neglected for *setup 3* ($\psi_{\text{RX}} = 5.1^\circ \Rightarrow \cos \psi_{\text{RX}} = 0.996$) but not for *setup 2* ($\psi_{\text{RX}} = -25.9^\circ \Rightarrow \cos \psi_{\text{RX}} = 0.900$). Therefore, the larger phase offset associated with a detuned *setup 2* ($\cos[5.1^\circ]/\cos[-25.9^\circ] \approx 1.107$) explains the increased τ_{RD} compared to *setup 3* ($\tau_{\text{RD}}[3]/\tau_{\text{RD}}[2] = 26.5/23.8 \approx 1.113$). The alternative saturation-recovery approach leads to consistent findings (Figure 5 and Table 2; $\cos[4.7^\circ]/\cos[-28.3^\circ] \approx 1.132$). Despite this agreement, different limitations affect the accuracy of both experiments: Saturation-recovery acquisitions may suffer from system instabilities (e.g., B_0 drifts, eddy currents), isochromat simulations (data not shown) indicate that the single-vector model may fail for $\theta > 90^\circ$, in line with previous results.⁹ With improved field homogeneity, such deviations become smaller and are negligible.

4.3 | RD during transmission

Results of the RADDEX measurements are shown in Figure 6A,B. Improved stability of the fits was achieved by

fitting all data from the four excitation schemes simultaneously. Damping during signal acquisition was neglected as only the magnitude of the summed spectra was considered in the fits yielding the following parameters: ζ_{TX} , ψ_{TX} , T_2 , δf , and c_{B1} . As in the free-precession case, the δf was used to correct for B_0 drifts, whereas the scaling factor c_{B1} corrects for B_1^+ deviations. Of note, relaxation during transmission is better approximated by T_2 instead of T_2^* used in the free-precession experiments.^{65,66} Results are also in Table 2.

The compensation of RD-related flip-angle deviations during runtime of a simple pulse-and-acquire sequence is demonstrated in Figure 6C,D showing the normalized signal magnitude as a function of the amplitude of a rectangular pulse of constant duration. The different version of the Tx/Rx switch ($R_1 = 49 \Omega$) was used in these experiments, leading to a higher reference voltage ($\approx 5\times$) to avoid discretization effects at long τ_p . Results of corresponding RADDEX measurements are provided as Figure S3, Table S1. Similar to Figure 2, the performance of the 360° pulse was not affected. Without correction, oscillations were distorted, especially around a 180° pulse, where RD effects are enhanced. Efficient mitigation is evident if $\tau_{\text{RD,TX}}$ and ψ_{TX} are properly considered in the amplitude- and pulse-modulated pulse. Overestimation of RD leads to opposite bias, whereas a subtle underestimation appeared benign. This suggests a

TABLE 2 Summary of the results obtained with the flip angle-array and saturation-recovery measurements during free precession as well as with RADDEX during transmission.

		Coil setup 1	Coil setup 2	Coil setup 3
Inserted cable		-	$\lambda/6$	$\lambda/4$
Damping effect		Minimal	Moderate	Maximal
Flip-angle array	$(\zeta_{\text{RX}}M_0)^{-1}/\text{ms}$	-	22.9 ± 0.2	21.5 ± 0.2
	$\Psi_{\text{RX}}/^\circ$	-	-25.9 ± 0.8	5.1 ± 0.3
	T_2^*/ms	-	38.0 ± 0.3	38.5 ± 0.2
	$\delta f/\text{Hz}$	-	0.8 ± 0.1	-0.5 ± 0.1
Saturation rec.	$(\zeta_{\text{RX}}M_0)^{-1}/\text{ms}$	-	24.4 ± 0.2	22.1 ± 0.2
	$\Psi_{\text{RX}}/^\circ$	-	-28.3 ± 0.6	4.7 ± 0.3
	T_2^*/ms	-	33.6 ± 0.2	34.4 ± 0.2
	$\delta f/\text{Hz}$	-	3.0 ± 0.1	-0.7 ± 0.1
RADDEX	$(\zeta_{\text{TX}}M_0)^{-1}/\text{ms}$	-	17.38	17.04
	$\Psi_{\text{TX}}/^\circ$	-	-24.03	-5.82
	T_2/ms	-	57.5	58.1
	$\delta f/\text{Hz}$	-	2.34	1.11
	c_{BI}	-	0.994	0.996

Note: The 19 mm sample was used for all acquisitions.

Abbreviation: RADDEX, radiation damping difference excitation.

certain tolerance in practical applications of the correction.

4.4 | RD in relaxation measurements

Simulations of VFA experiments and fits to Eq. (9) are presented in Figure 7. Remarkably, T_1 was slightly overestimated even in the absence of RD, despite the assumption of noise-free acquisitions. Absolute deviations (2 and 22 ms for the 0.5 ms and 5-ms pulse, respectively) did not vary significantly with intrinsic T_1 but increased with pulse duration. This is explained by relaxation during the pulse, which is considered in Eqs. (7a)–(7c) (i.e., in the simulations), but not in the fit function, Eq. (9). Therefore, θ_{eff} is reduced, and the T_1 overestimation increases with τ_p due to increasing relaxation effects. Simulated VFA experiments with shorter pulses ($\tau_p = 5 \mu\text{s}$; data not shown) confirmed this interpretation, yielding deviations <0.1 ms from ground truth. In contrast to T_1 overestimation due to unaccounted relaxation, RD caused T_1 underestimation by 0.7% and 7% for the 0.5 ms and the 5 ms pulse, respectively. Notably, both relaxation and RD lead to reduced θ_{eff} . However, relaxation causes rather uniform re-scaling, whereas the impact from RD is flip-angle dependent.

Figure 8 presents T_2 measurements (19 mm sample) with different echo spacings. Apparent deviations

from mono-exponential echo decays were not evident (Figure 8B,C). For the undamped case (*setup 1*), estimated T_2 times decreased monotonically from 60.5 ms ($\Delta\text{TE} = 9$ ms) to 59.7 ms ($\Delta\text{TE} = 20$ ms). This may be explained by increasing diffusion-related echo attenuation with longer ΔTE . A varying influence of pulse imperfections may also contribute to this observation.⁵¹ Similar results were obtained for the moderately damped case (*setup 2*), whereas deviations at longer ΔTE for the maximally damped *setup 3* suggested RD. Results for the 24 mm sample are shown as Figure S4, indicating larger T_2 deviations ($\approx 2\%$) for *setups 2* and *3*, consistent with enhanced RD due to increased η . Overall, while the high SNR supported the detection of RD effects, related T_2 deviations were smaller than those typically expected in repeated measurements due to subtle variations of the experimental conditions (e.g., temperature changes).

5 | DISCUSSION

This work demonstrates RD at a clinical field strength of 3T. Assuming that such effects are more common in experiments with dedicated coils for small samples, a Helmholtz coil was built that achieves a high η and Q , which are crucial requirements under such conditions. It also supports the generation of well-defined, short RF pulses ($\tau_p \geq$

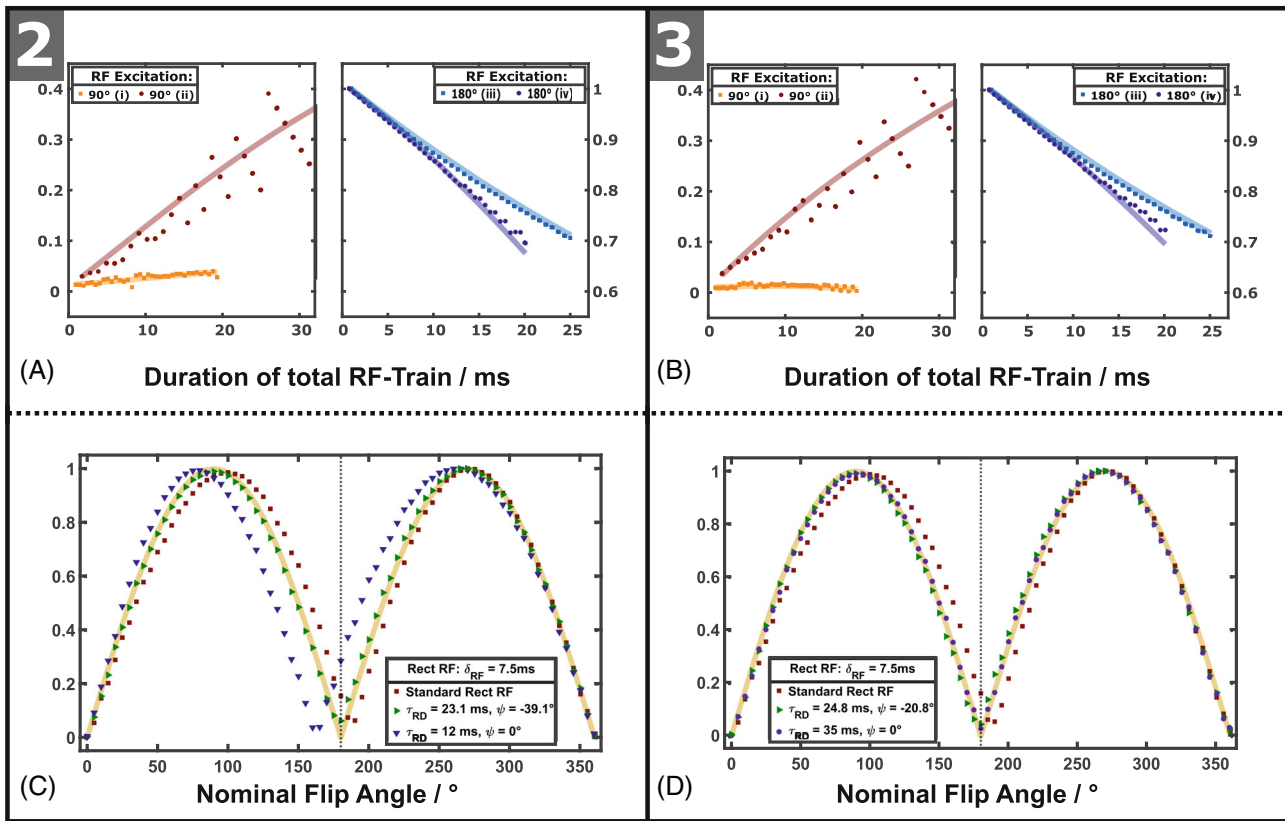


FIGURE 6 (A, B) Radiation damping difference excitation (RADDEX) experiments with the 19 mm sample and *coil setups 2* (moderately damped; A) and *3* (maximally damped; B). The signal magnitude (normalized to the signal after preparation with a 180° composite pulse of minimal duration) is plotted as a function of the composite pulse duration. Orange, red, light blue, and dark blue symbols refer to preparations by an “undamped” 90°, a “damped” 90°, an “undamped” 180°, and a “damped” 180° composite pulse, respectively. Corresponding solid lines indicate simultaneous NNLS fits to the combined data. Considerable radiation damping (RD) effects, which increase with pulse duration, lead to deviations from a normalized signal of 0 (after 90° preparation) or 1 (after 180° preparation) in all experiments, but are more pronounced for the “damped” preparations. An undesired effect of the discretization of the transmitter voltage is visible as a step function of data points acquired with longer pulse durations due to the relatively small reference voltage. (C, D) Demonstration of the online correction of a 7.5 ms rectangular RF pulse during runtime. Normalized signal intensities obtained with “pulse amplitude arrays” and *coil setups 2* (C) and *3* (D) are shown. As in Figure 2, the 360° pulse is minimally affected by RD. The uncorrected pulse (red squares) yields a shift of the minimum toward higher nominal flip angles. Results obtained with a corrected pulse shape based on a RADDEX acquisition (green triangles) follow an undistorted sinusoidal oscillation (indicated by the yellow line) and a minimum at half the amplitude of the 360° pulse. An overcorrection (use of a too short $\tau_{RD, TX}$ due to overestimation of RD; dark blue triangles in C) produces a minimum shift toward the opposite direction, whereas a moderate underestimation (dark blue circles in D) still yields an acceptable correction.

20 μ s), allowing to investigate RD or other nuisance effects over a wide range of pulse durations. Passive feedback integrated in the coil setup largely suppressed RD following the established concept of preamplifier decoupling. Alternatively, maximization or, more generally, modulation of RD was achieved by integrating coaxial cables of suitable length between the coil and the Tx/Rx switch. In combination, this allowed a comprehensive characterization of the spin-coil system and RD effects during excitation and free precession.

Results obtained with pulse-width arrays demonstrate substantial lineshape distortions if RD is not suppressed in the setup. This may compromise flip-angle calibration procedures, which are typically based on an automated

adjustment of a reference voltage for a 180° pulse on clinical scanners. Resulting flip-angle errors are non-linear, and maximal errors are expected for a 180° pulse, whereas a 360° pulse is almost unaffected. Consequently, they are not well corrected by rescaling employing B_1^+ mapping. Residual RD may, therefore, impact quantitative MR, such as VFA-based T_1 measurements. Our simulations indicate only small errors for $\tau_p \leq 1$ ms. Significantly longer pulses of potentially high amplitude are often used in MT imaging,^{37,67,68} or CEST.^{58,69} Integration of RD suppression approaches may, hence, be beneficial in such experiments.

T_2 measurements appeared to be relatively immune to RD-related perturbations. This robustness of spin-echo sequences can be explained by the absence of RD when

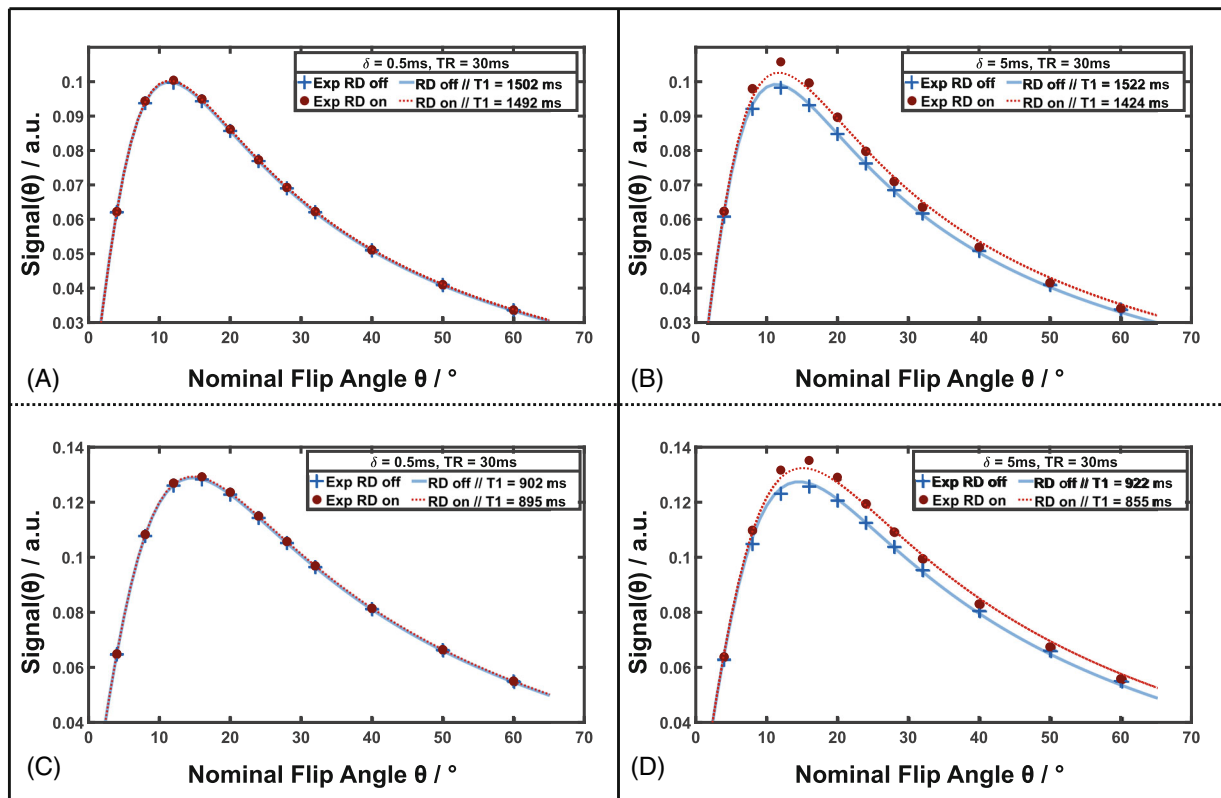


FIGURE 7 Simulations of variable flip angle (VFA) acquisitions with short ($\tau_p = 0.5$ ms; A, C) and long ($\tau_p = 5$ ms; B, D) rectangular pulses and typical relaxation times for gray matter ($T_1 = 1500$ ms, $T_2 = 100$ ms; A, B) and white matter ($T_1 = 900$ ms, $T_2 = 70$ ms; C, D). Blue crosses and red circles indicate calculated flip angle-dependent steady-state signals without ($\tau_{RD, TX} \rightarrow \infty$) and with relaxation damping ($\tau_{RD, TX} = 17$ ms), respectively. Blue solid and red dotted lines show corresponding fits to Eq. (9). Subtle overestimation of T_1 results even in the absence of RD due to relaxation during pulse application, which is enhanced for longer τ_p (A: 1502 ms; B: 1522 ms; C: 902 ms; D: 922 ms). By contrast, radiation damping (RD) leads to an increasing underestimation of T_1 with increasing τ_p (A: 1492 ms; B: 1424 ms; C: 895 ms; D: 855 ms).

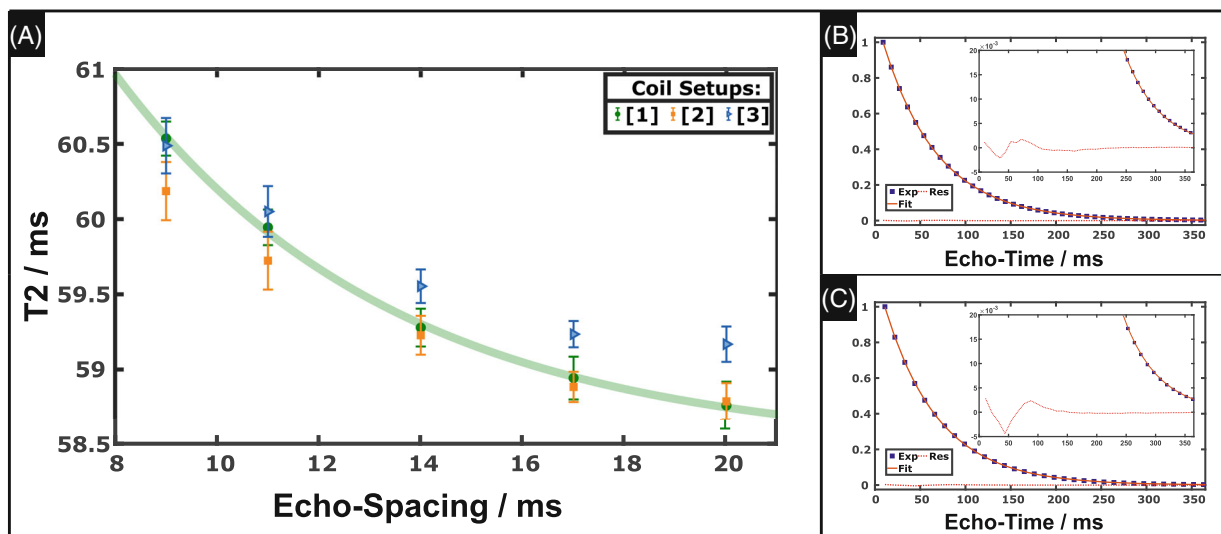


FIGURE 8 (A) Experimental estimations of T_2 in the 19 mm sample as a function of the echo-spacing in a Carr-Purcell-Meiboom-Gill (CPMG) sequence. Green circles, orange squares, and blue triangles show the results obtained with *coil setups 1, 2, and 3*, respectively. Error bars indicate ± 1 SD. The green solid line shows an exponential fit to the undamped data (*coil setup 1*). A subtle deviation from the undamped result is visible at the longest echo spacing for the maximally damped case. Exemplary fits to the normalized echo amplitudes recorded with *coil setup 1* (B; $\Delta TE = 9$ ms) and *coil setup 2* (C; $\Delta TE = 11$ ms) do not indicate relevant deviations from a mono-exponential decay or the occurrence of stimulated echoes. The insets of (B, C) show the data with a scaled y-axis.

nuclear spins are out of phase in an inhomogeneous field as already discussed by Bloembergen and Pound.⁴ Only experiments with $\Delta TE \geq 20$ ms indicated small T_2 errors, being more pronounced for larger η . This ΔTE is of the order of $\tau_{RD,RX}$ (23.8 and 12.0 ms for *setup 3* and the 19 and 24 mm sample, respectively; Table 1) supporting previous assumptions¹⁹ that RD effects in CPMG sequences may be ignored if $\Delta TE/\tau_{RD,RX} \ll 1$. Given current gradient limitations on clinical scanners, TE is typically long in diffusion-weighted experiments. While diffusion-sensitizing gradients would suppress RD, they are not applied in acquisitions with $b = 0$, which are, hence, more susceptible if RD is not mitigated in the coil setup.

Despite agreement with earlier observations, it remains unclear to what extent T_2 discrepancies can be attributed solely to RD. For a comprehensive analysis, an extension of the single-vector model to a distribution of isochromats would be required.⁴¹ Alternatively, we demonstrate experimental quantification of RD, allowing an assessment of whether perturbations must be accounted for in a specific measurement or how their impacts can be mitigated. For a general evaluation, it is recommended to use ratios T_2/τ_{RD} or T_2^*/τ_{RD} comparing the damping-field duration to the lifetime of coherence of the spin system. The latter ratio also appears to be more robust against erroneous T_2^* values if RADD SY experiments are analyzed without further ME-GRE data, as correlation between T_2^* and τ_{RD} limits accurate measurements of both parameters. Our results suggest that the damping rate and phase relation during free precession and transmission may deviate (Table 2), which has not been thoroughly studied before. Previous experiments with a small dual-loop coil indicated a higher coil current in the Tx mode due to a reduced fraction of reflected power.⁷⁰ A correspondingly increased mismatch of i_{in} and i_{re} leads to less efficient cancellation and, hence, reduced RD suppression, which is consistent with our results of $\zeta_{Tx}M_0 > \zeta_{Rx}M_0$ (58.7 vs. 45.9 s⁻¹, respectively, for coil *setup 3*; Table 2). Finally, the assumption of a perfectly tuned coil ($\psi = 0$) may not hold, which can lead to errors in the estimated damping time constant if unconsidered.

6 | CONCLUSIONS

Radiation damping may impact MR investigations of small tissue samples with dedicated RF coils and should be considered, especially in cases when precise quantification of MR parameters, such as relaxation rates, is required. Difference experiments comparing results with maximum and minimum RD impact provide a comprehensive quantitative characterization. Efficient mitigation can be

achieved hardware-based with a preamplifier decoupling approach or sequence-based with suitable RF pulse or gradient schemes. Simple VFA or multi-echo experiments are relatively robust against RD as long as pulse durations or echo spacings are short compared to the damping time constant.

ACKNOWLEDGEMENT

Open Access funding enabled and organized by Projekt DEAL.

FUNDING INFORMATION

This work was supported by the International Max Planck Research School on Neuroscience of Communication: Function, Structure, and Plasticity (IMPRS-NeuroCom).

CONFLICT OF INTEREST STATEMENT

The authors declare no potential conflict of interests.

DATA AVAILABILITY STATEMENT


Binary code of all pulse sequences used in the current work can be made available for use at other institutions on compatible scanners. Note that pulse sequences implemented with IDEA (Integrated Development Environment for Applications; Siemens Healthineers) contains vendor-specific code. Therefore, sharing sequence code can only take place via the customer-to-customer partnership program (so-called C2P procedure).

ORCID

Niklas Wallstein  <https://orcid.org/0009-0003-4952-7962>

Roland Müller  <https://orcid.org/0009-0009-0072-4002>

André Pampel  <https://orcid.org/0000-0002-9319-5016>

Harald E. Möller  <https://orcid.org/0000-0002-5659-1925>

TWITTER

Harald E. Möller  [HaraldMoeller](#)

REFERENCES

- Hoult DI, Richards RE. The signal-to-noise ratio of the nuclear magnetic resonance experiment. *J Magn Reson*. 1976;24:71-85.
- Hoult DI, Lauterbur PC. The sensitivity of the zeugmatographic experiment involving human samples. *J Magn Reson*. 1979;34:425-433.
- Suryan G. Nuclear magnetic resonance and the effect of the methods of observation. *Curr Sci*. 1949;18:203-204.
- Bloembergen N, Pound RV. Radiation damping in magnetic resonance experiments. *Phys Rev*. 1954;95:8-12.
- Bloom S. Effects of radiation damping on spin dynamics. *J Appl Phys*. 1957;28:800-805.
- Vlassenbroek A. *Radiation Damping in High Resolution NMR*. Ph.D. thesis. Université libre de Bruxelles; 1993.

7. Warren WS, Hammes SL, Bates JL. Dynamics of radiation damping in nuclear magnetic resonance. *J Chem Phys*. 1989;91:5895-5904.
8. Jeener J. Dipolar field and radiation damping: collective effects in liquid-state NMR. *eMagRes*. John Wiley & Sons; 2007.
9. Augustine MP. Transient properties of radiation damping. *Prog Nucl Magn Reson Spectrosc*. 2002;40:111-150.
10. Desvaux H. Non-linear liquid-state NMR. *Prog Nucl Magn Reson Spectrosc*. 2013;70:50-71.
11. Krishnan VV, Murali N. Radiation damping in modern NMR experiments: Progress and challenges. *Prog Nucl Magn Reson Spectrosc*. 2013;68:41-57.
12. Pelupessy P. Radiation damping strongly perturbs remote resonances in the presence of homonuclear mixing. *Magn Reson*. 2022;3:43-51.
13. Mao XA, Guo JX, Ye CH. Nuclear-magnetic-resonance line-shape theory in the presence of radiation damping. *Phys Rev B*. 1994;49:15702-15711.
14. Vlassenbroek A, Jeener J, Broekaert P. Radiation damping in high resolution liquid NMR: a simulation study. *J Chem Phys*. 1995;103:5886-5897.
15. Barfuss H, Fischer H, Hentschel D, et al. In vivo magnetic resonance imaging and spectroscopy of humans with a 4 T whole-body magnet. *NMR Biomed*. 1990;3:31-45.
16. Zhou JY, Mori S, van Zijl PCM. FAIR excluding radiation damping (FAIRER). *Magn Reson Med*. 1998;40:712-719.
17. Wu DH, Johnson CS. Radiation-damping effects on relaxation-time measurements by the inversion-recovery method. *J Magn Reson A*. 1994;110:113-117.
18. Mao XA, Guo JX, Ye CH. Radiation damping effects on spin-lattice relaxation time measurements. *Chem Phys Lett*. 1994;222:417-421.
19. Mao XA, Guo JX, Ye CH. Radiation damping effects on transverse relaxation time measurements. *Chem Phys Lett*. 1994;227:65-68.
20. Sklenar V. Suppression of radiation damping in multidimensional NMR experiments using magnetic field gradients. *J Magn Reson A*. 1995;114:132-135.
21. Bayle K, Julien M, Remaud GS, Akoka S. Suppression of radiation damping for high precision quantitative NMR. *J Magn Reson*. 2015;259:121-125.
22. Williamson DC, Närväinen J, Hubbard PL, Kauppinen RA, Morris GA. Effects of radiation damping on Z-spectra. *J Magn Reson*. 2006;183:203-212.
23. Guéron M. A coupled resonator model of the detection of nuclear magnetic resonance: radiation damping, frequency pushing, spin noise, and the signal-to-noise ratio. *Magn Reson Med*. 1991;19:31-41.
24. Müller N, Jerschow A. Nuclear spin noise imaging. *Proc Natl Acad Sci U S A*. 2006;103:6790-6792.
25. Chen J-H, Jerschow A, Bodenhausen G. Compensation of radiation damping during selective pulses in NMR spectroscopy. *Chem Phys Lett*. 1999;308:397-402.
26. Huang SY, Witzel T, Wald LL. Accelerated radiation damping for increased spin equilibrium (ARISE): a new method for controlling the recovery of longitudinal magnetization. *Magn Reson Med*. 2008;60:1112-1121.
27. Barjat H, Mattiello DL, Freeman R. Suppression of radiation damping in high-resolution NMR. *J Magn Reson*. 1999;136:114-117.
28. Anklin C, Rindlisbacher M, Otting G, Laukien FH. A probehead with switchable quality factor. Suppression of radiation damping. *J Magn Reson B*. 1995;106:199-201.
29. Broekaert P, Jeener J. Suppression of radiation damping in NMR in liquids by active electronic feedback. *J Magn Reson A*. 1995;113:60-64.
30. Xu X, Lee JS, Jerschow A. Ultrafast scanning of exchangeable sites by NMR spectroscopy. *Angew Chem Int ed Engl*. 2013;52:8281-8284.
31. Khittrin AK, Jerschow A. Simple suppression of radiation damping. *J Magn Reson*. 2012;225:14-16.
32. Keeler A, Whitney HM. Characterization and suppression techniques for degree of radiation damping in inversion recovery measurements. *Spectrosc Lett*. 2015;48:781-786.
33. Rourke DE, Augustine MP. Exact linearization of the radiation-damped spin system. *Phys Rev Lett*. 2000;84:1685-1688.
34. Lapert M, Assémat E, Glaser SJ, Sugny D. Optimal control of the signal-to-noise ratio per unit time of a spin $\frac{1}{2}$ particle: the crusher gradient and the radiation damping cases. *J Chem Phys*. 2015;142:044202.
35. Möller HE, Bossoni L, Connor JR, et al. Iron, myelin, and the brain: neuroimaging meets neurobiology. *Trends Neurosci*. 2019;42:384-401.
36. Stüber C, Morawski M, Schäfer A, et al. Myelin and iron concentration in the human brain: a quantitative study of MRI contrast. *Neuroimage*. 2014;93:95-106.
37. Marschner H, Pampel A, Müller R, et al. High-resolution magnetization-transfer imaging of post-mortem marmoset brain: correlations with relaxometry and histology. *Neuroimage*. 2023;268:119860.
38. Pampel A, Müller DK, Anwander A, Marschner H, Möller HE. Orientation dependence of magnetization transfer parameters in human white matter. *Neuroimage*. 2015;114:136-146.
39. Kauppinen RA, Thothard J, Leskinen HPP, et al. Axon fiber orientation as the source of T1 relaxation anisotropy in white matter: a study on corpus callosum. *Magn Reson Med*. 2023;90:708-721.
40. Lu H, Clingman C, Golay X, van Zijl PCM. Determining the longitudinal relaxation time (T1) of blood at 3.0 tesla. *Magn Reson Med*. 2004;52:679-682.
41. Augustine MP, Hahn EL. Radiation damping with inhomogeneous broadening: limitations of the single Bloch vector model. *Concepts Magn Reson*. 2001;13:1-7.
42. Wallstein N, Müller R, Pampel A, Möller HE. Radiation damping at clinical field strengths: how to analyse and avoid it to enable quantitative MRI with dedicated coils. In Proceedings of the 31st Annual Meeting of ISMRM, Toronto, ON, Canada; 2023:1241.
43. Thangavel K, Saritas EU. Aqueous paramagnetic solutions for MRI phantoms at 3 T: a detailed study on relaxivities. *Turk J Electr Eng Comp Sci*. 2017;25:2108-2121.
44. Müller R, Wallstein N, Pampel A, Möller HE. A 3T Helmholtz coil with either reduced or maximized radiation damping effects. In Proceedings of the 31st Annual Meeting of ISMRM, Toronto, ON, Canada; 2023:5278.

45. Hoult DI, Deslauriers R. Elimination of signal strength dependency upon coil loading—an aid to metabolite quantitation when the sample volume changes. *Magn Reson Med.* 1990;16:418-424.
46. Roemer PB, Edelstein WA, Hayes CE, Souza SP, Mueller OM. The NMR phased array. *Magn Reson Med.* 1990;16:192-225.
47. Hoult DI, Bhakar B. NMR signal reception: virtual photons and coherent spontaneous emission. *Concepts Magn Reson.* 1997;9:277-297.
48. Marion DJY, Desvaux H. An alternative tuning approach to enhance NMR signals. *J Magn Reson.* 2008;193:153-157.
49. Pöschko MT, Schlagnitweit J, Huber G, et al. On the tuning of high-resolution NMR probes. *Chem Phys Chem.* 2014;15:3639-3645.
50. Keifer PA. 90° pulse width calibrations: how to read a pulse width array. *Concepts Magn Reson.* 1999;11:165-180.
51. Poon CS, Henkelman RM. Practical T2 quantitation for clinical applications. *J Magn Reson Imaging.* 1992;2:541-553.
52. Szantay C, Demeter A. Radiation damping diagnostics. *Concepts Magn Reson.* 1999;11:121-145.
53. Guéron M, Leroy JL. NMR of water protons. The detection of their nuclear-spin noise, and a simple determination of absolute probe sensitivity based on radiation damping. *J Magn Reson.* 1989;85:209-215.
54. Huang SY, Anklin C, Walls JD, Lin YY. Sizable concentration-dependent frequency shifts in solution NMR using sensitive probes. *J Am Chem Soc.* 2004;126:15936-15937.
55. Garwood M, Ke Y. Symmetrical pulses to induce arbitrary flip angles with compensation for Rf inhomogeneity and resonance offsets. *J Magn Reson.* 1991;94:511-525.
56. Levitt MH. Symmetrical composite pulse sequences for NMR population inversion. I. Compensation of radiofrequency field inhomogeneity. *J Magn Reson.* 1982;48:234-264.
57. Müller DK, Pampel A, Möller HE. Matrix-algebra-based calculations of the time evolution of the binary spin-bath model for magnetization transfer. *J Magn Reson.* 2013;230:88-97.
58. Lenich T, Pampel A, Mildner T, Möller HE. A new approach to Z-spectrum acquisition: prospective baseline enhancement (PROBE) for CEST/nuclear Overhauser effect. *Magn Reson Med.* 2019;81:2315-2329.
59. Fram EK, Herfkens RJ, Johnson GA, et al. Rapid calculation of T1 using variable flip angle gradient refocused imaging. *Magn Reson Imaging.* 1987;5:201-208.
60. Helms G, Dathe H, Dechent P. Quantitative FLASH MRI at 3T using a rational approximation of the Ernst equation. *Magn Reson Med.* 2008;59:667-672.
61. Wansapura JP, Holland SK, Dunn RS, Ball WS Jr. NMR relaxation times in the human brain at 3.0 tesla. *J Magn Reson Imaging.* 1999;9:531-538.
62. Stanisz GJ, Odobina EE, Pun J, et al. T1, T2 relaxation and magnetization transfer in tissue at 3T. *Magn Reson Med.* 2005;54:507-512.
63. Wright PJ, Mougou OE, Totman JJ, et al. Water proton T1 measurements in brain tissue at 7, 3, and 1.5 T using IR-EPI, IR-TSE, and MPRAGE: results and optimisation. *Magn Reson Mater Phys.* 2008;21:121-130.
64. Ernst RR, Anderson WA. Application of Fourier transform spectroscopy to magnetic resonance. *Rev Sci Instrum.* 1966;37:93-102.
65. Torrey HC. Transient nutations in nuclear magnetic resonance. *Phys Rev.* 1949;76:1059-1068.
66. Wheaton AJ, Borthakur A, Corbo MT, Moonis G, Melhem E, Reddy R. T_{2ρ}-weighted contrast in MR images of the human brain. *Magn Reson Med.* 2004;52:1223-1227.
67. Wolff SD, Balaban RS. Magnetization transfer contrast (MTC) and tissue water proton relaxation in vivo. *Magn Reson Med.* 1989;10:135-144.
68. Sled JG. Modelling and interpretation of magnetization transfer imaging in the brain. *Neuroimage.* 2018;182:128-135.
69. Ward KM, Aletas AH, Balaban RS. A new class of contrast agents for MRI based on proton chemical exchange dependent saturation transfer (CEST). *J Magn Reson.* 2000;143:79-87.
70. Darrasse L, Kassab G. Quick measurement of NMR-coil sensitivity with a dual-loop probe. *Rev Sci Instrum.* 1993;64:1841-1844.

SUPPORTING INFORMATION

Additional supporting information may be found in the online version of the article at the publisher's website.

Table S1. Summary of the results obtained with radiation damping difference excitation (RADDEX) (19 mm sample) and the alternative Tx/Rx switch configuration with $R_1 = 49 \Omega$ and $R_2 = 1 \Omega$.

Figure S1. Free induction decay signal recorded with a simple pulse-and-acquire sequence with different flip angles.

Figure S2. Circuit diagram of the Tx/Rx switch.

Figure S3. Results from radiation damping difference excitation (RADDEX) experiments (19 mm sample) and the alternative Tx/Rx switch configuration with $R_1 = 49 \Omega$ and $R_2 = 1 \Omega$.

Figure S4. Results from experimental estimations of T_2 in the 24 mm sample as a function of the echo-spacing in a Carr-Purcell-Meiboom-Gill (CPMG) sequence.

How to cite this article: Wallstein N, Müller R, Pampel A, Möller HE. Radiation damping at clinical field strength: Characterization and compensation in quantitative measurements. *Magn Reson Med.* 2023;1-15. doi: 10.1002/mrm.29934